Modification of the structure of diamond with MeV ion implantation

Modification of structural and mechanical properties of diamond with MeV ion implantation

F.Bosia[1], N.Argiolas[2], M.Bazzan[2], P.Olivero[1], F.Picollo[1], A.Sordini[3], M.Vannoni[3], H.Wang[1], E.Vittone[1].

[1]*Dept. Experimental Physics- NIS Centre of Excellence, Università di Torino, INFN Torino, Italy*

[2] *Dept. Physics, Università di Padova, Italy*

Abstract

We present experimental results and numerical simulations to investigate the modification of structural-mechanical properties of ion-implanted single-crystal diamond. A phenomenological model is used to derive an analytical expression for the variation of mass density and elastic properties as a function of damage density in the crystal. These relations are applied together with SRIM Monte Carlo simulations to set up Finite Element simulations for the determination of internal strains and surface deformation of MeV-ion-implanted diamond samples. The results are validated through comparison with High Resolution X-ray Diffraction and white-light interferometric profilometry experiments. The former are carried out on 180 keV B implanted diamond samples, to determine the induced structural variation, in terms of lattice spacing and disorder, whilst the latter are performed on 1.8 MeV He implanted diamond samples to measure surface swelling. The effect of thermal processing on the evolution of the structural-mechanical properties of damaged diamond is also evaluated by performing the same profilometric

measurements after annealing at 1000 °C, and modeling the obtained trends with a suitably modified analytical model. The results allow the development of a coherent model describing the effects of MeV-ion-induced damage on the structural-mechanical properties of single-crystal diamond. In particular, we suggest a more reliable method to determine the so-called diamond “graphitization threshold” for the considered implantation type.

Keywords

Ion implantation; Damaged diamond; Graphitization; Annealing; Mechanical deformation; X-Ray Diffraction, Numerical analysis

1. Introduction

Considerable effort has been devoted in recent years to the application of high energy (MeV) ion implantation in the fabrication and functionalization of diamond, in particular with the aim of developing a series of micro-devices, ranging from bio-sensors and detectors to micro-electromechanical systems (MEMS) and optical devices [1-5]. This can be achieved by exploiting the strongly non-uniform damage depth profile of MeV ions and creating specific regions where the diamond lattice structure is critically damaged. After annealing, graphitization of the buried layer is achieved whilst the remaining surrounding material is restored to pristine diamond, so that spatially well-defined structures can be created by subsequently etching away the graphitized regions [6] or advantage can be taken of the conductive properties of the graphitized regions [5, 7].

In order to control the spatial extension of the graphitized layer with some accuracy, it is necessary to acquire in depth knowledge of how the diamond lattice structure is modified as a function of implanted ion type, energy, fluence, implantation temperature, annealing temperature, local stress, etc. In particular, a critical damage level N_C has been identified in the literature, above which diamond is subject to permanent amorphization and subsequent graphitization upon thermal annealing [8], although some uncertainty remains on the value of N_C and its dependence on implantation parameters (e.g. depth and/or local strain, self-annealing, etc) [2, 9-12].

A well-known effect of ion implantation in diamond is surface swelling in correspondence with the irradiated regions, due to the internal density variation in the damaged crystal, which causes a constrained volume expansion [13-15]. A detailed

analysis of this effect can provide additional information on the structural modifications occurring in ion-implanted diamond. This type of study was the object of investigation in [16], where a phenomenological model accounting for saturation in vacancy density was developed, and Finite-Element (FEM) Simulations were performed to compare numerical results with experimental surface swelling measurements. In this paper, we extend the numerical procedure to model annealing effects in ion-implanted specimens, introducing the concept of a graphitization threshold in a rigorous analysis. To validate the model, the results of simulations were compared with surface swelling profilometry measurements and with High Resolution X-ray Diffraction (HR-XRD) analyses.

The paper is structured as follows: in Section 2, the model for structural variation of damaged diamond is reviewed and extended to annealed specimens; in Section 3, experimental and numerical techniques are presented; in Section 4, HR-XRD and profilometric measurements are presented and discussed, and the numerical fitting of experimental swelling results is carried out.

2. Model

We adopt the model presented in [16], which accounts for saturation in the creation of vacancies in the damaged diamond crystal lattice for increasing fluencies in ion implantation. The vacancy density of the damaged diamond as a function of substrate depth z and implantation fluence F can be expressed as:

$$\rho_V(F,z) = \alpha\left(1 - e^{-\frac{\lambda(z)F}{\alpha}}\right) \tag{1}$$

where the constant α represents the vacancy density saturation value, which depends on the implantation type, and λ is the linear vacancy depth profile calculated using the SRIM 2008.04 code [17]. The corresponding mass density ρ of the damaged diamond is:

$$\rho(F,z) = \rho_d - (\rho_d - \rho_{aC})\left(1 - e^{-\frac{\lambda(z)F}{\alpha}}\right) \quad (2)$$

where ρ_d =3.52 g cm^{-3} is the diamond density and ρ_{aC} =1.56 g cm^{-3} is the amorphous carbon density [18]. Similarly for the substrate Young's modulus:

$$E(F,z) = E_d - (E_d - E_{aC})\left(1 - e^{-\frac{\lambda(z)F}{\alpha}}\right) \quad (3)$$

with E_d =1220 GPa and E_{aC} =10 GPa [18], and Poisson's ratio:

$$\nu(F,z) = \nu_d - (\nu_d - \nu_{aC})\left(1 - e^{-\frac{\lambda(z)F}{\alpha}}\right) \quad (4)$$

with ν_d =0.2 and ν_{aC} =0.45 [18].

When damaged diamond is annealed between 1000°-1200°C, the crystal lattice is almost completely restored to that of pristine diamond if the vacancy density is below the so-called graphitization threshold N_C, whilst there is a transition to the structure and properties of graphite for material portions above N_C. Therefore, to determine the density depth profile for a given implanted substrate, one must compare the corresponding vacancy density profile with the graphitization threshold N_C. An example is shown in Fig.

1 for 1.8 MeV He^+ implantations at fluences of F_1=1.4·10^{16} ions cm^{-2} and F_2=10.5·10^{16} ions cm^{-2}. For the implantation fluence F_1, the damage density curve $\rho_V(z)$ lies entirely below N_C ("below threshold" in Fig. 1), and the structural/mechanical properties before annealing are given by Eqs.2-4, whilst after annealing they are restored to those of diamond. For the implantation fluence F_2, the damage density curve has a peaked damage density lying above N_C ("above threshold" in Fig. 1), and the structural/mechanical properties before annealing are again given by Eqs. 2-4, whilst after annealing they are converted to those of graphite (i.e. ρ_g = 1.80 g cm^{-3}, E_g = 20 GPa, ν_g = 0.2 g cm^{-3}) for $\rho_V(z)>N_C$ and restored to those of diamond for $\rho_V(z)<N_C$.

3. Experimental and numerical techniques

3.1. Samples and ion implantation

Ion implantation was performed on HPHT (produced by Sumitomo, type Ib, 100 crystal orientation) and CVD (produced by ElementSix, type IIa, 100 crystal orientation) samples, 3×3×1.5 mm^3 and 3×3×0.5 mm^3 in size, respectively, with two optically polished opposite large faces. The two sample types, HPHT and CVD, can be reasonably expected to display the same high-quality single-crystal mechanical properties.

In order to use the HR-XRD technique, diamond samples with relatively shallow damage profiles are required, because thick profiles (>μm) would give diffraction spectra characterized by very rapid angular variations of the intensity, which are difficult to analyze with standard HR-XRD equipment. Therefore, the first (CVD) sample was implanted with 180 keV B ions, at the Olivetti I-Jet facilities in Arnad (Aosta, Italy)

obtaining a profile which extends to about 600 nm in depth. The whole upper surface of the sample was irradiated uniformly with a fluence of 10^{13} ions cm^{-2}.

The second (HPHT) sample was irradiated with 1.8 MeV He ions at the ion microbeam line of the INFN Legnaro National Laboratories (Padova, Italy). Typically, ~125×125 μm^2 square areas were implanted by raster scanning an ion beam with size of 20-30 μm. The implantation fluences, ranging from $1 \cdot 10^{16}$ ions cm^{-2} to $2 \cdot 10^{17}$ ions cm^{-2}, were controlled in real time by monitoring the X-ray yield from a thin metal layer evaporated on the sample surface. The implantations were performed at room temperature, with ion currents of ~1 nA.

3.2. HR-XRD measurements

Boron-implanted samples were investigated with the HR-XRD technique at the department of Physics of the University of Padova. The instrument used is a Philips MRD diffractometer. The source is an X-ray tube with copper anode, equipped with a parabolic mirror and a Ge (2 2 0) Bartels monochromator with four bounces. The resulting primary beam has a divergence angle of 0.0039° and a spectral purity of $\Delta\lambda / \lambda = 10^{-5}$ at a wavelength λ = 1.54056 Å. The beam impinges on the sample at an angle ω measured by a high precision goniometer, on which the specimen is mounted. The scattered radiation from the sample is measured as a function of the incidence angle ω and the scattering angle 2θ by a Xe proportional detector mounted on a second independent goniometer, coaxial to the first. To improve the resolution of the angular measurement, the detector is equipped with a Ge (2 2 0) analyzer with three rebounds that

guarantees acceptance angle of 0.0039°. The system is maintained in a measuring chamber at a constant temperature of (25.0 ± 0.1) °C [19].

The unimplanted and implanted HPHT and CVD samples are measured under the same conditions near the (0 0 4) reflection. The measurement consists in a ω-2θ scan so that the incidence and collection angles are varied in a synchronized manner. This kind of scan is sensitive to deformations along the surface normal [19]. Moreover, in order to characterize the presence of substrate curvature, the lateral size of the primary beam is reduced to 0.1 mm using a slit and a series of ω – scans are performed as a function of the sample position. In this case the detector is kept fixed and the sample is rotated. For details see ref. [19].

3.3. Profilometry measurements

Surface swelling data were acquired at the Interferometry laboratories of the Istituto Nazionale di Ottica (INO), Firenze, with a Zygo NewView 6000 system, which exploits white light interferometry to provide detailed, non contact measurements of 3-D profiles [20]. A vertical resolution of 0.1 nm was achieved over a lateral range up to 150 μm, while lateral resolution varied from 4.6 μm up to 0.6 μm, depending on the objective.

3.4. FEM simulations

Simulations were carried out using “Structural mechanics” module COMSOL Multiphysics, as explained in [16]. Specimen geometry is reproduced and meshed in 2-D

simulations. The analytical expressions for density and mechanical parameters of the substrate given by Eq. 2-4 are used to model specimens before annealing, together with the damage profile $\lambda(z)$ resulting from SRIM simulations for 180 keV B and 1.8 MeV He, with a displacement energy of a carbon atom in diamond of 50 eV [21]. The saturation value for vacancy density α for the two implantation types are extrapolated by best fitting procedures to be $\alpha_{180\ keV\ B}= 8\cdot10^{22}$ ions cm^{-2} and $\alpha_{1.8\ MeV\ He}=7\cdot10^{22}$ ions cm^{-2} (see Section 4.2). For annealed specimens, the step-like density and mechanical parameter depth variation illustrated in Fig.1 is used. For both implantations types, surface deformation and internal strains are calculated as a function of the irradiation fluence.

4. Results and discussion

4.1. HR-XRD measurements

In Figure 2a we report the ω-2θ rocking curve for unimplanted diamond substrates acquired in proximity of the 0 0 4 reciprocal lattice point. From the comparison between the two substrates and a reference calculation, it can be seen that both the substrates are characterized by a large FWHM value. As this is several times larger than the theoretical peak width calculated on the basis of the dynamical theory of X-ray diffraction [19] corrected for experimental broadening, it indicates the presence of some kind of structural disorder in the substrate prior to implantation. A series of ω–scans as a function of the beam position on the sample reveals that this is due to bending of the lattice planes in the sample [22]: the maximum curvature is found near the sample edges and can be estimated to have a radius of about 32 m. Thus, the substrates are affected prior to the

implantation by the presence of slowly varying structural disorder, probably caused by the presence of residual thermal stresses which deform the sample, and result in a wider Bragg peak in HR-XRD measurements.

A reciprocal space map for the as- implanted samples with B at 180 keV (not shown) acquired in proximity of the asymmetric 1 1 3 reflection provides evidence for implantation–induced deformation, with no relaxation occurring at the interface between the implanted region and the underlying substrate. The deformation is positive, i.e. the implantation provokes lattice expansion, as expected. The ω-2θ scan acquired along the symmetrical 0 0 4 lattice point for the substrate implanted with a fluence of 10^{13} ions cm^{-2} is reported in Figure 2b. The shoulder appearing on the left of the Bragg peak indicating the presence of lattice expansion [19] is clearly visible. Using the relations explained in Section 2, the relative density variation and strain as a function of depth can be estimated and compared to the expected lattice mismatch, as calculated by HR-XRD. In order to check this aspect, the experimental rocking curves are compared to a simulation based on the dynamical theory of X-rays diffraction [19] assuming a proportionality relation between the vacancy defect profile obtained using Eq. (1) and the deformation one. The mismatch profile was approximated with a step function using 10 lamellae with thicknesses of 30 nm, and the proportionality constant was adjusted by hand until a reasonable agreement was obtained. The obtained value of the proportionality constant is equal to 2.2×10^{-24} and its meaning is the contribution of each vacancy to the relative mismatch. The agreement between simulated and experimental profiles is only qualitative (Fig. 2b), because the above–mentioned curvature of the substrate smears out the spectrum details and broadens the peaks, while the simulation assumes a perfect substrate

with a depth–only dependent deformation. In any case from this comparison we can estimate an order of magnitude for the relative lattice mismatch induced by the implantation process, which is in the 10^{-4} –10^{-3} range and has a positive sign (i.e. the lattice expands, as anticipated by the reciprocal lattice map analysis).

4.2. Surface swelling measurements

Experimental surface swelling data for 1.8 MeV He implantations for fluences varying between 10^{16} ions cm^{-2} and $2.5 \cdot 10^{17}$ ions cm^{-2} before and after annealing at 1000 °C are compared to simulation data. Experimental measurements show that after annealing the swelling values decrease and tend to zero for small fluences (below F=$1.4 \cdot 10^{16}$ ions cm^{-2}), and the opposite occurs in the large fluence range. As pointed out in [23], this indicates that for fluences below this threshold value, annealing at 1000 °C causes a near complete restoration of the pristine diamond crystal, whilst for fluences above this value graphitization induces a greater swelling. This observation can be exploited to determine N_C from eq.(1), as the vacancy density value corresponding to the threshold fluence value. A value of $N_C \cong 2 \cdot 10^{22}$ vacancies cm^{-3} is therefore estimated for 1.8 MeV He implantations. This value is consistent with previous measurements cited in the literature for different types of implantations (ion types and energies) [8, 9, 11, 15, 23, 24], and is somewhat smaller than expected for measurements relative to similar implantations [2], while being closer to the values reported by the previously cited references. The reason for this could be the approach described in Section 2, where saturation effects are duly accounted for in the vacancy density for increasing fluence, as expressed by Eq.(1). This

effect was not considered in the determination of N_C in previous literature. The derived parameter N_C is therefore used in FEM simulations.

Figure 3 shows experimentally measured and numerically calculated surface swelling profiles for F=4.18·10^{16} ions cm^{-2}. For this above-threshold fluence value, swelling increases after specimen annealing. Numerical simulations capture this behavior very satisfactorily.

Figure 4 shows the variation of experimental and numerically calculated swelling values as a function of fluence F, before and after annealing. Error bars for experimental data are estimated at ±5% on fluence values and ±5nm on displacement values. The best fit of numerical data for samples before annealing is obtained for $\alpha_{1.8\ \mathrm{MeV\ He}}$ = 7·10^{22} vac cm^{-3} , which is a correction on previously reported values [16], due to the wider fluence range considered for the fit on experimental data. Numerical data fit experimental values very satisfactorily in the low-fluence range, whilst there is some discrepancy for higher fluences. This could be due to the simplified assumptions in deriving Eq.(1), which is based on a linear relationship between the recombination probability for a vacancy in a damage cascade and the vacancy density itself [16]. Further data analysis on a greater number of implantation examples is needed to address this issue.

Conclusions

This experimental-numerical study, based on a phenomenological model accounting for saturation in the vacancy density in ion-implanted diamond, yields good accordance between measured and calculated data. Qualitative and preliminary quantitative

confirmation of the approach is obtained through HR-XRD measurements of ion-implanted diamond specimens.

The effect of specimen annealing is also considered: We show that analysis of experimental data, together with due consideration for the corrected vacancy density profile, allows the reliable determination of a diamond graphitization threshold for a given implantation type. In the considered case, numerical simulations based on this graphitization threshold value also show good accordance with experimental data. The proposed approach shows promise for a systematic study of a greater number of cases, in order to determine the dependency of the graphitization threshold from various implantation parameters.

Acknowledgments

The authors wish to thank Dr. Paolo Schina for specimen preparation at the Olivetti I-JET facilities at Arnad (Aosta). This work is supported by the “Accademia Nazionale dei Lincei – Compagnia di San Paolo” Nanotechnology grant” and by “DANTE” and “FARE” experiments of “Istituto Nazionale di Fisica Nucleare” (INFN), which are gratefully acknowledged.

References

[1] P. Olivero, S. Rubanov, P. Reichart, B.C. Gibson, S.T. Huntington, J. Rabeau, A.D. Greentree, J. Salzman, D. Moore, D.N. Jamieson, S. Prawer, Ion-beam-assisted lift-off technique for three-dimensional micromachining of freestanding single-crystal diamond. Advanced Materials, 17 (2005) 2427.

[2] P. Olivero, S. Rubanov, P. Reichart, B.C. Gibson, S.T. Huntington, J.R. Rabeau, A.D. Greentree, J. Salzman, D. Moore, D.N. Jamieson, S. Prawer, Characterization of three-dimensional microstructures in single-crystal diamond. Diamond and Related Materials, 15 (2006) 1614-1621.

[3] P. Olivero, G. Amato, F. Bellotti, O. Budnyk, E. Colombo, M. Jaksic, C. Manfredotti, Z. Pastuovic, F. Picollo, N. Skukan, M. Vannoni, E. Vittone, Direct fabrication of three-dimensional buried conductive channels in single crystal diamond with ion microbeam induced graphitization. Diamond and Related Materials, 18 (2009) 870-876.

[4] B.A. Fairchild, P. Olivero, S. Rubanov, A.D. Greentree, F. WaIdermann, R.A. Taylor, I. Walmsley, J.M. Smith, S. Huntington, B.C. Gibson, D.N. Jamieson, S. Prawer, Fabrication of Ultrathin Single-Crystal Diamond Membranes. Advanced Materials, 20 (2008) 4793.

[5] A.I. Sharkov, T.I. Galkina, A.Y. Klokov, R.A. Khmelnitskii, V.A. Dravin, A.A. Gippius, High-speed bolometric detector based on a graphitized layer buried into bulk diamond. Vacuum, 68 (2002) 263-267.

[6] N.R. Parikh, J.D. Hunn, E. McGucken, M.L. Swanson, C.W. White, R.A. Rudder, D.P. Malta, J.B. Posthill, R.J. Markunas, Single-crystal diamond plate liftoff achieved by

ion implantation and subsequent annealing. Applied Physics Letters, 61 (1992) 3124-3126.

[7] F. Picollo, P. Olivero, F. Bellotti, Z. Pastuovic, N. Skukan, A. Lo Giudice, G. Amato, M. Jaksic, E. Vittone, Formation of buried conductive micro-channels in single crystal diamond with MeV C and He implantation. Diamond and Related Materials, 19 (2010) 466-469.

[8] C. Uzansaguy, C. Cytermann, R. Brener, V. Richter, M. Shaanan, R. Kalish, Damage Threshold for Ion-Beam-Induced Graphitization of Diamond. Applied Physics Letters, 67 (1995) 1194-1196.

[9] A.A. Gippius, R.A. Khmelnitskiy, V.A. Dravin, S.D. Tkachenko, Formation and characterization of graphitized layers in ion-implanted diamond. Diamond and Related Materials, 8 (1999) 1631-1634.

[10] D.P. Hickey, K.S. Jones, R.G. Elliman, Amorphization and graphitization of single-crystal diamond - A transmission electron microscopy study. Diamond and Related Materials, 18 (2009) 1353-1359.

[11] R. Kalish, A. Reznik, K.W. Nugent, S. Prawer, The nature of damage in ion-implanted and annealed diamond. Nuclear Instruments & Methods in Physics Research Section B-Beam Interactions with Materials and Atoms, 148 (1999) 626-633.

[12] J.F. Prins, T.E. Derry, Radiation defects and their annealing behaviour in ion-implanted diamonds. Nuclear Instruments & Methods in Physics Research Section B-Beam Interactions with Materials and Atoms, 166 (2000) 364-373.

[13] J.F. Prins, Derry, T.E., Sellschop, J.P.F. , Volume expansion of diamond during diamond implantation. Physical Review B 34 (1986).

[14] E.W. Maby, C.W. Magee, J.H. Morewood, Volume expansion of ion-implanted diamond. Applied Physics Letters, 39 (1981) 157-158.

[15] J.D. Hunn, S.P. Withrow, C.W. White, D.M. Hembree, Raman-Scattering from Mev-Ion Implanted Diamond. Physical Review B, 52 (1995) 8106-8111.

[16] F. Bosia, S. Calusi, L. Giuntini, S. Lagomarsino, A. Lo Giudice, M. Massi, P. Olivero, F. Picollo, S. Sciortino, A. Sordini, M. Vannoni, E. Vittone, Finite element analysis of ion-implanted diamond surface swelling. Nuclear Instruments and Methods in Physics Research Section B: Beam Interactions with Materials and Atoms, 268 (2010) 2991-2995.

[17] J.F. Ziegler, M.D. Ziegler, J.P. Biersack, SRIM - The stopping and range of ions in matter (2010). Nuclear Instruments & Methods in Physics Research Section B-Beam Interactions with Materials and Atoms, 268 (2010) 1818-1823.

[18] Y.X. Wei, R.J. Wang, W.H. Wang, Soft phonons and phase transition in amorphous carbon. Physical Review B, 72 (2005).

[19] P.F. Fewster, X-Ray Scattering from Semiconductors, Imperial College Press 2003.

[20] L. Deck, P. Degroot, High-Speed Noncontact Profiler Based on Scanning White-Light Interferometry. Applied Optics, 33 (1994) 7334-7338.

[21] W. Wu, S. Fahy, Molecular-Dynamics Study of Single-Atom Radiation-Damage in Diamond. Physical Review B, 49 (1994) 3030-3035.

[22] T. Bauer, M. Schreck, J. Hartwig, X.H. Liu, S.P. Wong, B. Stritzker, Structural defects in homoepitaxial diamond layers grown on off-axis Ib HPHT substrates. Physica Status Solidi a-Applications and Materials Science, 203 (2006) 3056-3062.

[23] A.V. Khomich, R.A. Khmelnitskiy, V.A. Dravin, A.A. Gippius, E.V. Zavedeev, I.I. Vlasov, Radiation damage in diamonds subjected to helium implantation. Physics of the Solid State, 49 (2007) 1661-1665.

[24] M.G. Allen, S. Prawer, D.N. Jamieson, R. Kalish, Pulsed-Laser Annealing of P-Implanted Diamond. Applied Physics Letters, 63 (1993) 2062-2064.

List of Figure Captions

Fig. 1: Top) Vacancy density vs. specimen depth for diamond implanted with 1.8 MeV He ions: two examples are shown for F_1=1.4·10^{16} ions cm^{-2} and F_2=10.5·10^{16} ions cm^{-2}, below and above the graphitization threshold, respectively; Below) corresponding mass density before and after annealing at 1000 °C.

Fig. 2: a) Comparison between rocking curves of the HPHT and CVD substrates and a reference simulation. (0 0 4) lattice planes. b) experimental and simulated rocking curves for the symmetrical 004 reflection for CVD sample implanted with B@180keV, 10^{13} ions/cm^2.

Fig. 3. Experimentally measured ("exp") and numerically computed ("num") surface swelling profiles *h(x)* before ("RT"=Room Temperature) and after annealing ("1000 C") for 1.8MeV He ions for F=4.18·10^{16} ions cm^{-2}

Fig. 4. Experimentally measured ("exp") and numerically computed ("num") surface swelling values *h* as a function of implantation fluence *F* before ("RT"=Room Temperature) and after annealing ("1000°") for He@1.8MeV ions.

Fig. 1

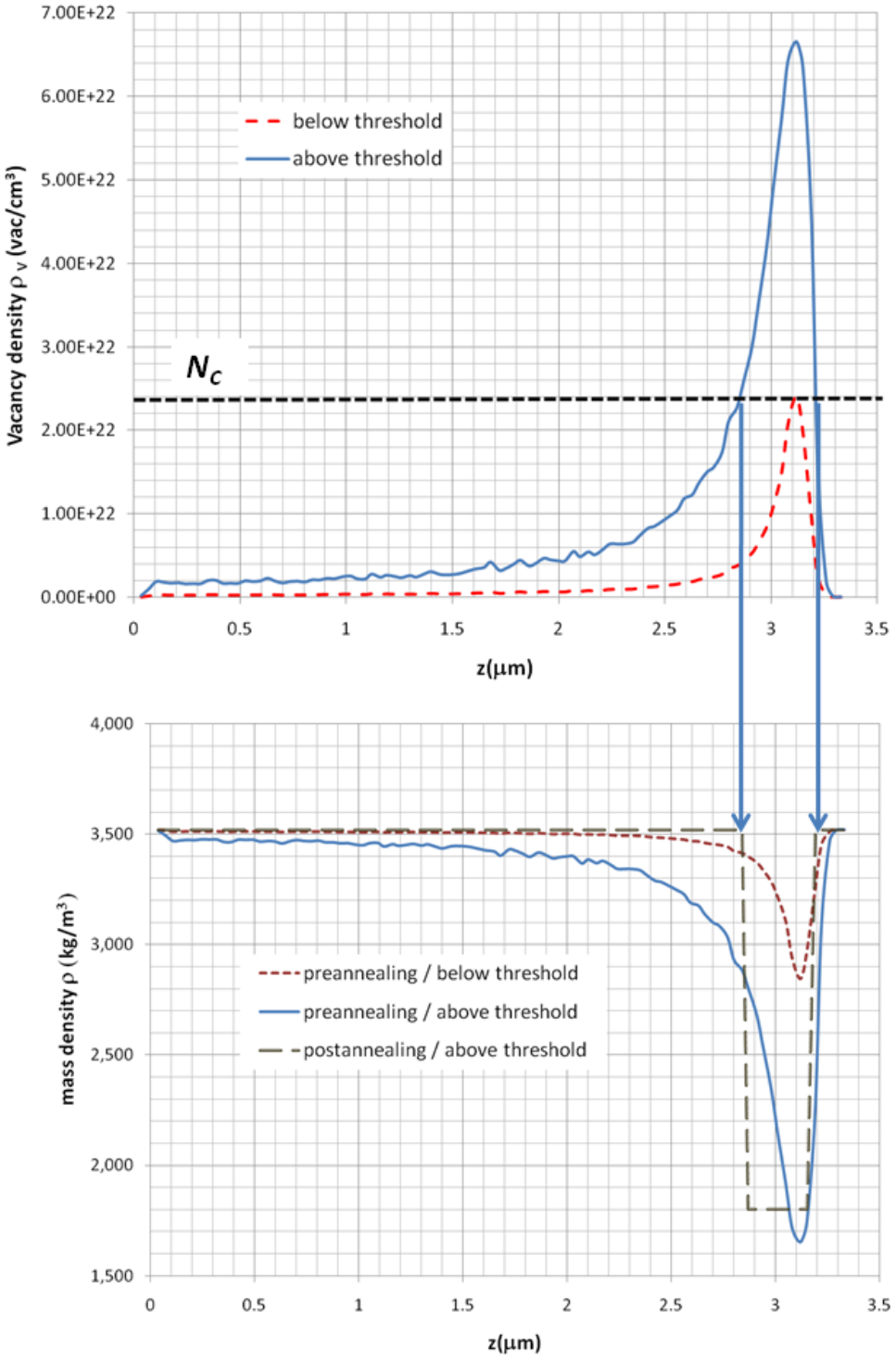
7.00E+22
6.00E+22
5.00E+22
4.00E+22
3.00E+22
2.00E+22
1.00E+22
0.00E+00
Vacancy density ρ v (vac/cm³)
below threshold
above threshold
Nc
0
0.5
1
1.5
2
2.5
3
3.5
z(μm)
4,000
3,500
3,000
2,500
2,000
1,500
mass density ρ (kg/m³)
preannealing / below threshold
preannealing / above threshold
postannealing / above threshold
0
0.5
1
1.5
2
2.5
3
3.5
z(μm)

Fig. 2

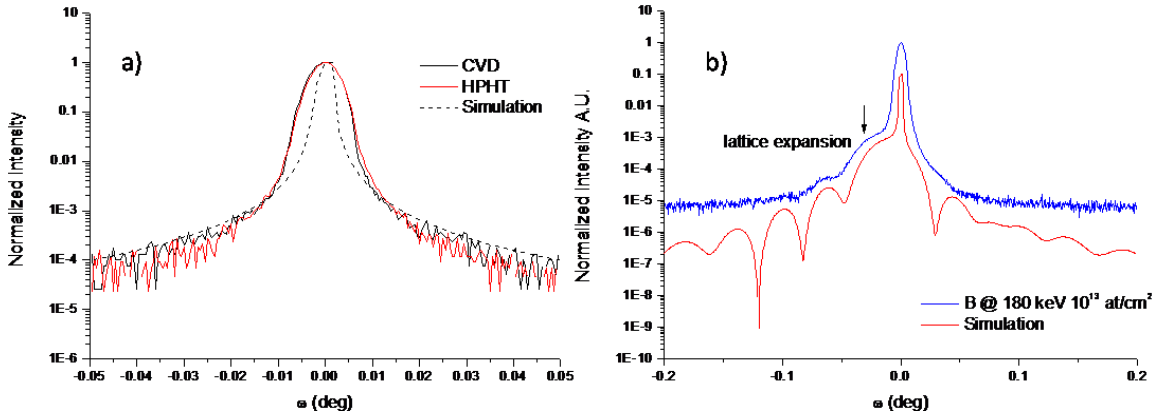
a)
CVD
HPHT
Simulation
Normalized Intensity
ω (deg)
b)
lattice expansion
B @ 180 keV 10^13 at/cm^2
Simulation
Normalized Intensity A.U.
ω (deg)

Fig. 3

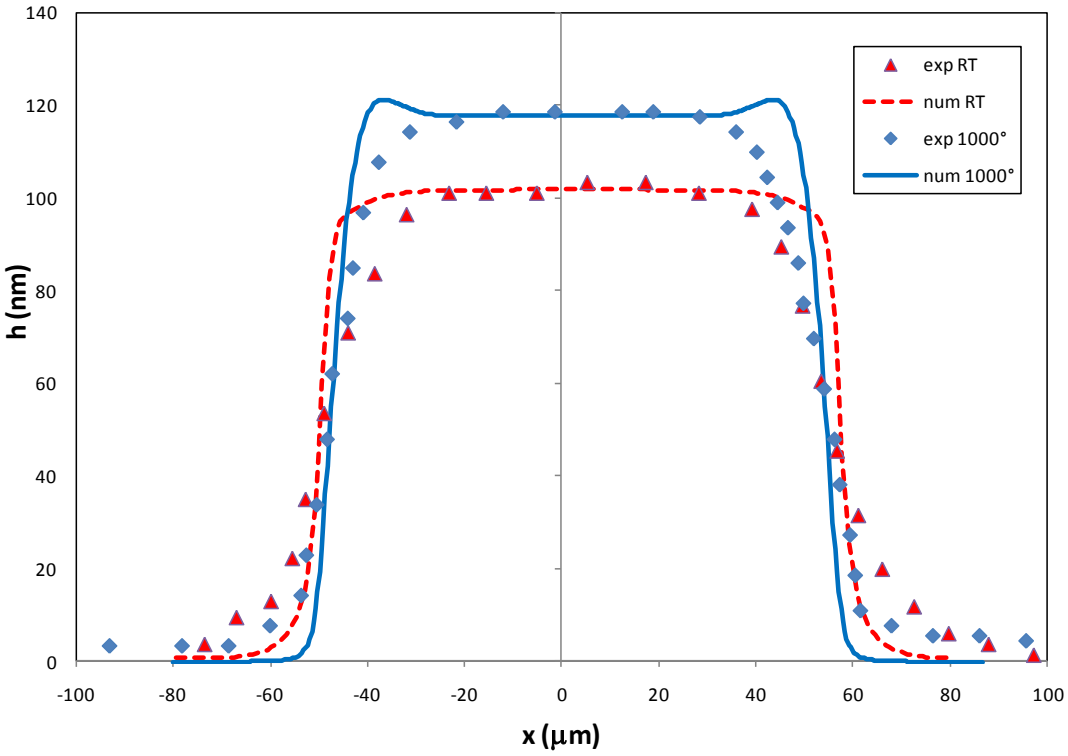
140
120
100
80
60
40
20
0
h (nm)
-100
-80
-60
-40
-20
0
20
40
60
80
100
x (µm)
exp RT
num RT
exp 1000°
num 1000°

Fig. 4

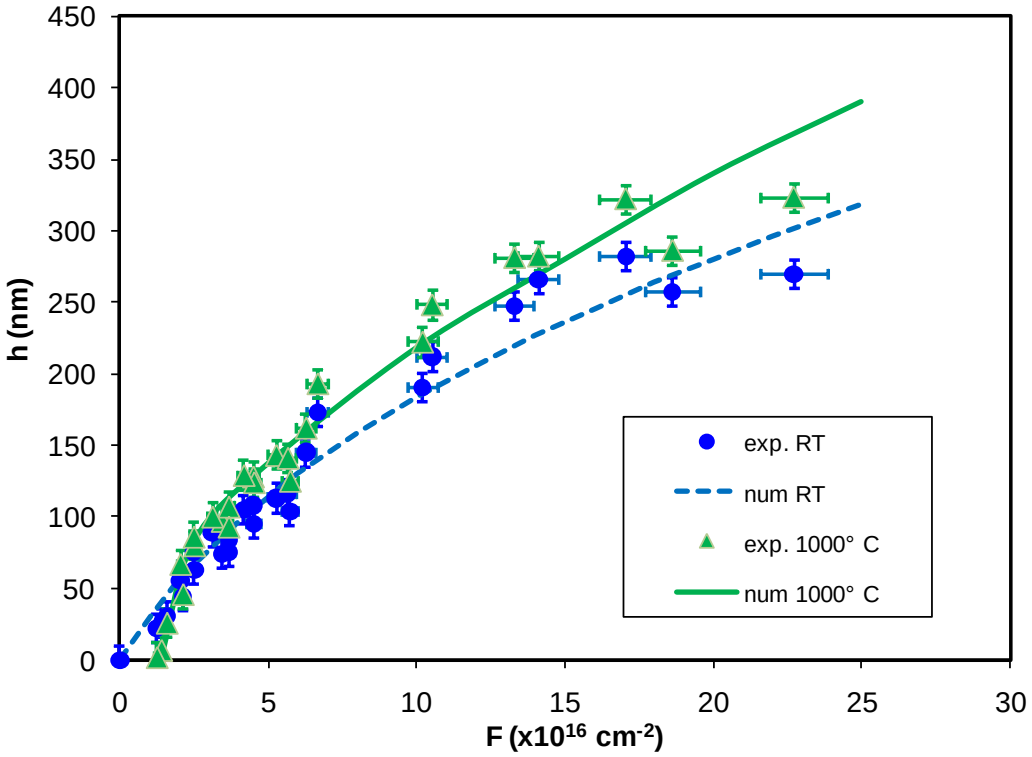
450
400
350
300
250
200
150
100
50
0
h (nm)
0
5
10
15
20
25
30
F (x10^16 cm^-2)
exp. RT
num RT
exp. 1000° C
num 1000° C

Figure 1

Click here to download high resolution image

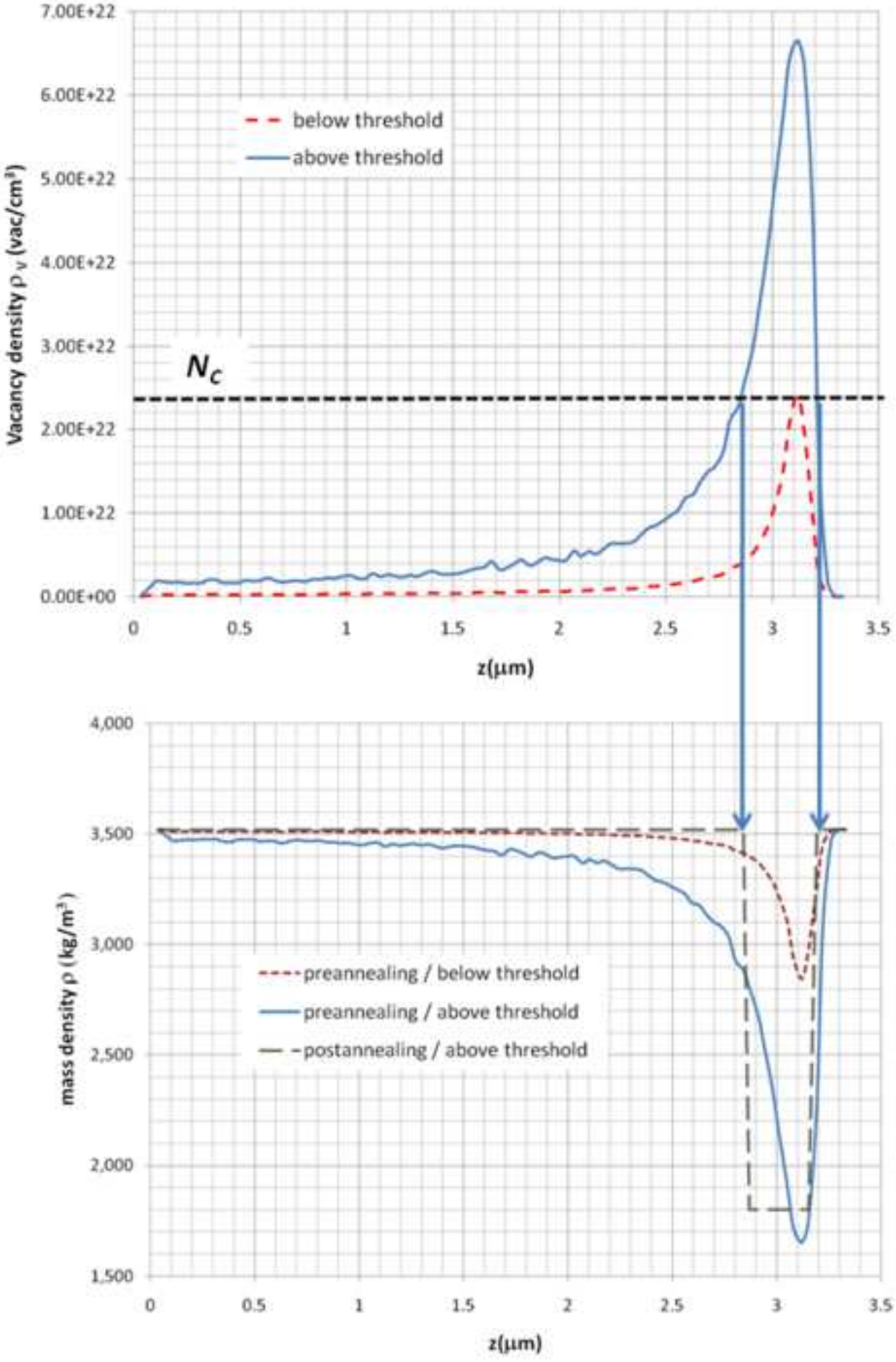

Figure 2a

Click here to download high resolution image

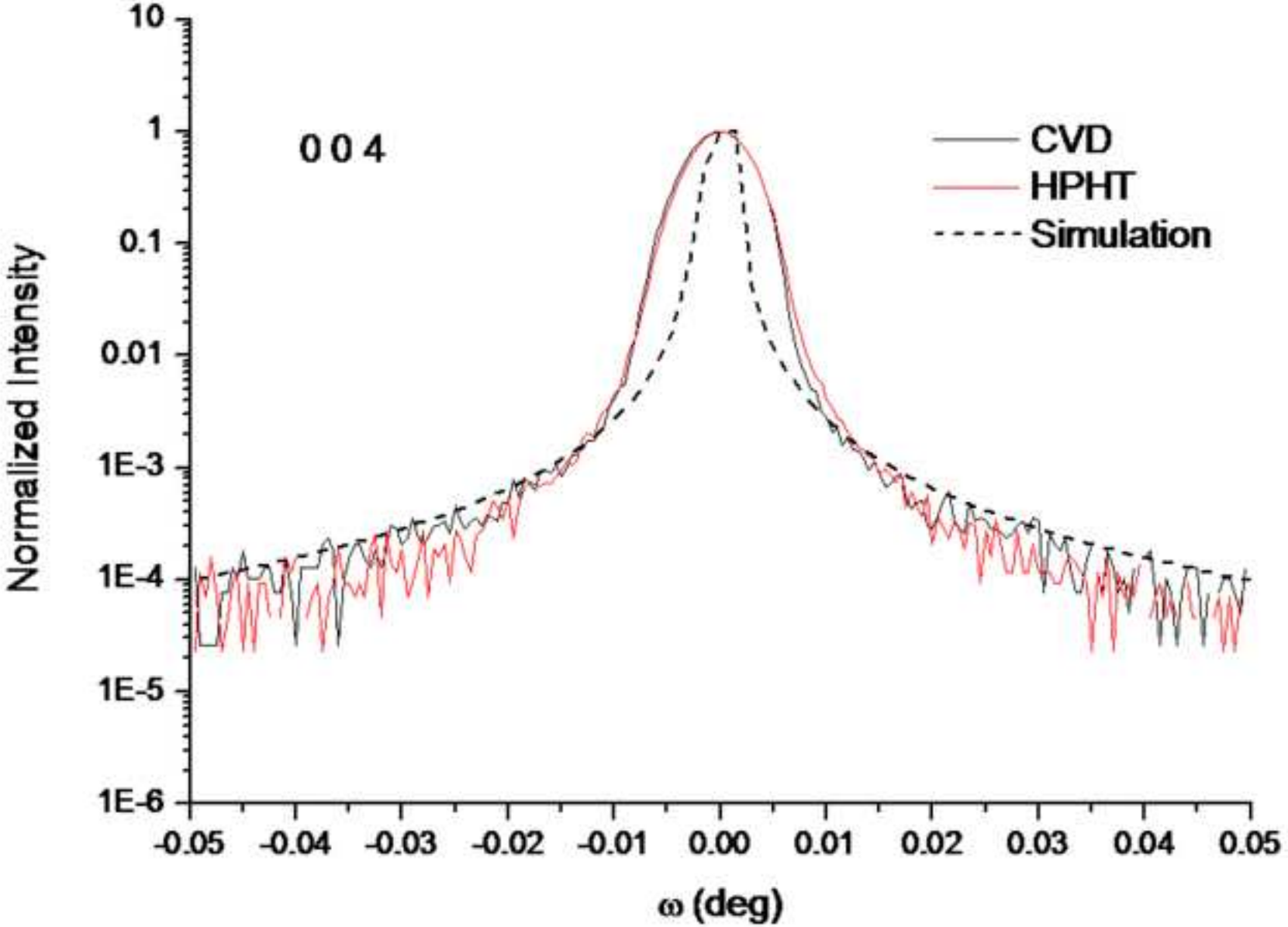

Figure 2b

Click here to download high resolution image

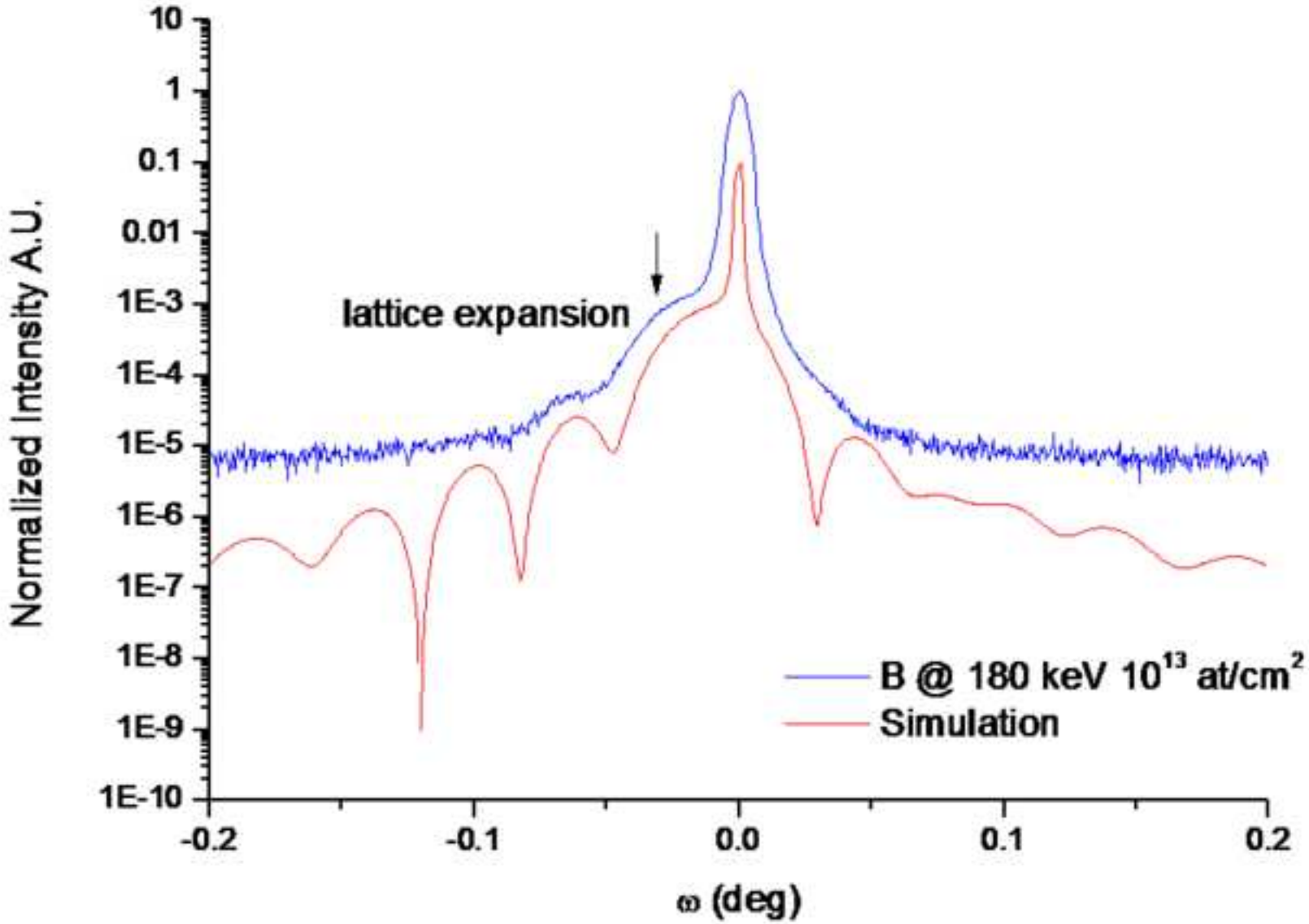

Figure 3

Click here to download high resolution image

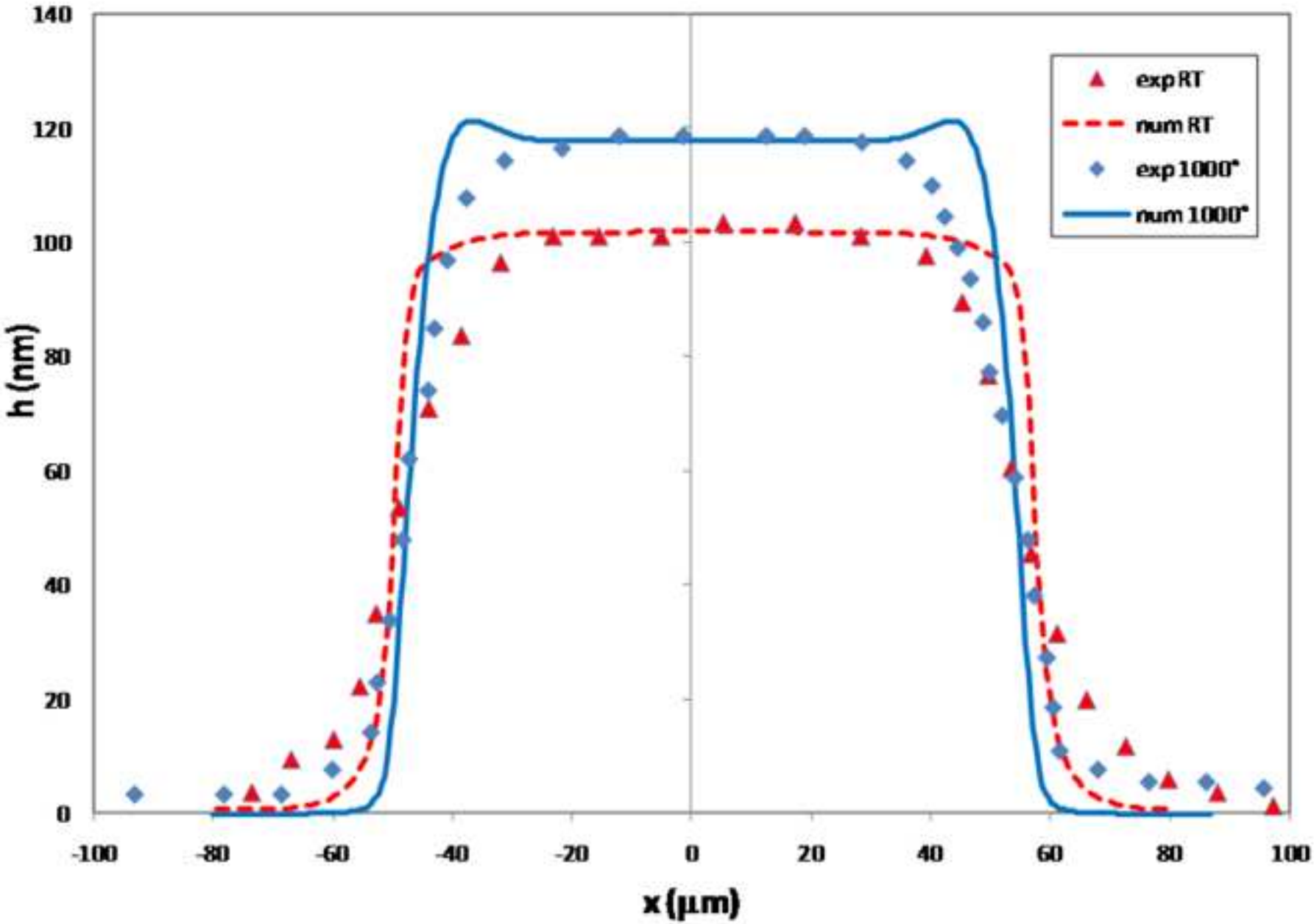

Figure 4

Click here to download high resolution image